THE PLANETARY SCIENCE JOURNAL, 6:197 (12pp), 2025 August https://doi.org/10.3847/PSJ/ade433


# The Mineralogical Connection between M- and K-type Asteroids as Indicated by Polarimetry

Joseph R. Masiero[1], Yuna G. Kwon[1], Elena Selmi[2], and Manaswi Kondapally[3]
[1] Caltech/IPAC, 1200 E California Blvd., MC 100-22, Pasadena, CA 91125, USA; jmasiero@ipac.caltech.edu
[2] Department of Physics, University of Oxford, Parks Rd., Oxford OX1 3PU, UK
[3] Department of Earth and Space Exploration (Astrophysics), Arizona State University, Tempe, AZ, USA
*Received 2025 April 18; revised 2025 June 5; accepted 2025 June 12; published 2025 August 20*

## Abstract

Polarimetry has the capacity to provide a unique probe of the surface properties of asteroids. Trends in polarization behavior as a function of wavelength trace asteroid regolith mineral properties that are difficult to probe without measurements in situ or on returned samples. We present recent results from our ongoing survey of near-infrared polarimetric properties of asteroids. Our data reveal a mineralogical link between asteroids in the broader M and K spectral classes. In particular, M-type objects (16) Psyche, (55) Pandora, (135) Hertha, and (216) Kleopatra show the same polarimetric-phase behavior as K-type objects (89) Julia, (221) Eos, and (233) Asterope from visible through near-infrared light. The near-infrared behavior for these objects is distinct from other classes observed to date, and shows a good match to the polarimetric properties of M-type asteroid (21) Lutetia from the visible to the near-infrared. The best link for these objects from laboratory polarimetric phase curve measurements is to a troilite-rich fine-grained regolith. Our observations indicate that the M- and K-type spectral classes are most likely part of a continuum, with the observed spectral differences due to heterogeneity from partial differentiation, shock darkening of the surface material, or other later evolution of the original parent population. We also provide incidental *J*- and *H*-band polarimetric observations of other main belt asteroids obtained during our survey.

*Unified Astronomy Thesaurus concepts:* Asteroids (72); Asteroid surfaces (2209); Polarimetry (1278)

## 1. Introduction

One of the fundamental outstanding questions in planetary science is: What is the history of protoplanetary differentiation in the solar system, and how many bodies underwent complete melting during formation? Observations of asteroids' sizes and masses have revealed ∼10 objects with densities consistent with iron-rich phases of a differentiated body (B. Carry 2012). Radar observations show reflectivities for objects like (16) Psyche and (216) Kleopatra are also consistent with metal-rich surfaces (S. Ostro et al. 2000; C. Neese et al. 2020). In contrast with this, isotopic analysis of iron meteorites (another line of evidence for differentiation in the early solar system) indicates that they sample many dozens of sources (T. H. Burbine et al. 2002) from a wide range of heliocentric distances (B. Zhang et al. 2024).

These various observations could all be consistent with a large original population of objects that differentiated early in the solar system's history and then were nearly all shattered before the majority of the material was removed. However, there is a notable absence of the other collisional products that would be expected to have been produced in such events, including the iron-poor residual mantle materials. Other than Vesta and its asteroid family, we see no evidence for the basaltic material that would form during the process of differentiation, often referred to as the "missing mantle" problem (J. F. Bell et al. 1989).

Spectroscopically, metal-rich asteroids have no significant features at visible or near-infrared wavelengths (S. J. Bus & R. Binzel 2002; F. E. DeMeo et al. 2009; M. Mahlke et al. 2022), while photometrically they tend to have moderate albedos both at visible and near-infrared wavelengths that fall between the larger C- and S complexes (A. K. Mainzer et al. 2011; J. Masiero et al. 2014). Polarimetric studies, however, offer a complementary way of studying these objects. By investigating the polarimetric-phase curves as a function of wavelength, we can probe compositional information that cannot be revealed from spectra or colors alone.

As sunlight interacts with asteroid surface materials during scattering, it can be imparted with a polarization. This polarization, which is usually below 2% for main belt asteroids, depends on the phase angle associated with scattering (the Sun-object-Earth angle), as well as the specific composition and distribution of the scattering elements on the surface (K. Muinonen et al. 2002; J. Masiero et al. 2009). The measurement of the polarization-phase curve of an asteroid can thus be used to probe the surface composition of the object in a way that is independent of, but complementary to, the results provided by photometry and spectroscopy (see S. Bagnulo et al. 2024 for a recent review). The visible to near-infrared wavelength regime spans the typical primary grain sizes expected of asteroid regolith, and polarization across these wavelengths can show significant changes tied to the surface properties (J. Masiero et al. 2023; Y. P. Bach et al. 2024).

In this work, we present recent results from our ongoing survey of asteroid near-infrared polarimetric phase curves. We focus on representative objects from two taxonomic classes: the M- and K classes, both of which show muted spectra and moderate albedos. As shown below, our observations demonstrate a link between these two classes, which stand apart from the behavior of other taxonomies observed to date.

## 2. Observations and Data Reduction

We obtained new near-infrared polarimetric observations of our targets using the Wide-field InfraRed Camera+Polarimeter (WIRC+Pol) on the Palomar 200 inch telescope (S. Tinyanont et al. 2019b). WIRC+Pol uses a combination quarter-wave plate and a polarizing grating to simultaneously obtain spectral traces of the four linear Stokes components ($+Q$, $-Q$, $+U$, and $-U$) at both $J$ and $H$ bands (1.25 and 1.64 $\mu$m, respectively). An upstream half-wave plate allows the Stokes vector sampled by each beam to be swapped, allowing for improved measurement precision, with accuracies of order 0.1% (S. Tinyanont et al. 2019a).

Our observing strategy follows the process described in J. Masiero et al. (2022) and J. Masiero et al. (2023). Following those works, we generally used A–B pointing positions for each target to enable improved background subtraction, and we obtain a minimum of four sequences of four half-wave plate rotations per pointing per band to mitigate any systematics. The exposure time for each image was scaled to the predicted brightness of the target at the time of observation, usually either 1 s (the minimum possible exposure time), 5 s, or 30 s. For all observations, the telescope was tracked at nonsidereal rates to maintain the target on approximately the same pixels for each pointing at all half-wave plate orientations.

We use the standard WIRC+Pol data reduction pipeline software[4] to correct the images for dark and flat-field effects, and to extract the degree and angle of polarization for each target. Dark frames were obtained at each of the exposure times used at the beginning and end of each night, and flat field images were obtained in both bands at the beginning and end of the night as well. Although WIRC+Pol obtains polarization measurements at a low spectral resolution across the entire bandpass, we perform an error-weighted coadd to derive a single measurement at each band to improve accuracy. Data from all obtained exposures of an object in a given band on each night are combined to produce the final polarization measurement of that object. Based on previous analyses, we add 0.1% in quadrature to the statistical uncertainty to account for residual systematic errors (J. Masiero et al. 2022), and add $7\overset{\circ}{.}8$ to the derived angle of polarization in both $J$ and $H$ bands to correct the observed offset (J. Masiero et al. 2023). Our final calibrated polarization measurements for the M- and K-type objects discussed here are presented in Table 1, while incidental observations obtained for other main belt asteroids are given in Table A1.

## 3. Results

We fit our observations with the polarimetric-phase relationship described in K. Muinonen et al. (2009), following the same implementation described in J. Masiero et al. (2023). The near-infrared polarimetric phase curves for M-type asteroids show a change in behavior from the $V$-band polarimetric phase curves fitted to data from the literature (D. Lupishko 2022).[5] Combining our observations for asteroids (16) Psyche, (55) Pandora, (135) Hertha, and (216) Kleopatra, we see a slightly deeper negative polarization branch ($P_{\min}$), a higher angle of minimum polarization ($\alpha_{\min}$), and a steeper slope at the inversion angle ($h$) (Figure 1), although our limited coverage of the positive polarization branch means that the slope differences may be due to the limited data set. Fit values for the polarimetric phase curves are given in Table 2 with 16th and 84th percentile uncertainties determined by looking at the range of fits for 100 Monte Carlo simulations of the polarimetric measurements, assuming the uncertainties follow a Gaussian behavior. Previous near-infrared (NIR) polarimetric results (J. Masiero et al. 2022, 2023) have shown that S-type asteroids show subtle changes from visual to NIR, and the "Barbarian" asteroids show significant changes, but neither class of objects shows changes similar to those observed here.

However, we find another asteroid taxonomy that is consistent with the M-type asteroid polarimetric phase curves at both visible and near-infrared wavelengths: the K-type asteroids (as shown in Table 2). Figure 2 shows the polarimetric phase curves for asteroids (89) Julia, (221) Eos, and (233) Asterope, while Figure 3 shows the M- and K-type objects plotted jointly. (221) Eos and its associated collisional family have previously been shown to have unique properties at infrared wavelengths in the form of a 3.4 $\mu$m albedo that is distinct from other observed families (J. Masiero et al. 2014) that has been interpreted to be a result of shock-darkening of the surface (J. Masiero et al. 2015). This is consistent with recent results from J. Sanchez et al. (2025) showing that increasing quantities of shock-darkened material added to meteorites will result in lower albedos across all wavelengths.

I. N. Belskaya et al. (2017) presented fits to the $V$-band polarimetric phase curves for both the M- and K classes. Their fitted $P_{\min}$ and $\alpha_{\min}$ are consistent with our fits to the full $V$-band literature data set shown in Table 2, while their $\alpha_0$ and $h$ slopes are offset from our fits, likely due to differences in coverage of the positive polarization branch. Alternatively, as the I. N. Belskaya et al. (2017) data include a larger set of objects for both classes, the difference in fits may indicate the presence of compositional (and thus polarimetric) variations within each class.

## 4. Discussion

During our analysis, we found that our NIR phase curves closely matched the $V$-band polarimetric phase curves for the M-type asteroid (21) Lutetia (fit parameters are shown in Table 2, and best-fit phase curve is shown in Figure 3). Lutetia was a flyby target for the ESA mission Rosetta (H. Sierks et al. 2011), which found a high-density, low-porosity body with an ancient surface that implies it has survived intact for the age of the solar system. Spectral measurements of Lutetia showed an absence of the 1 and 2 $\mu$m features that are associated with silicate compositions (A. Coradini et al. 2011). Lutetia is comparable in size to Eos, Asterope, and Pandora (sizes of $\sim$100 km). We obtained NIR polarimetric observations for Lutetia, which show a similar behavior to the $V$- and $i$-band data from the literature, as shown in Figure 4. The smaller change seen for Lutetia's polarimetric phase curve across wavelengths may be due to a difference in retained grain size distribution of the regolith, as was suggested to explain the effects seen for the "Barbarians" (J. Masiero et al. 2023).

Compared to laboratory spectra, our $J$- and $H$-band measurements are also consistent with the polarization-phase curve for the 20% olivine–80% troilite mixture obtained by R. Sultana et al. (2023a), as shown in Figure 5, while the $V$-band curve more closely matches their 10% olivine–90% troilite mixture. This may

[4] https://github.com/WIRC-Pol/wirc_drp

[5] Additional $V$-band observations for Psyche, Hertha, and Kleopatra were obtained from the Grupo de Ciencias Planetarias San Juan website: http://gcpsj.sdf-eu.org/catalogo.html.

**Table 1**
WIRC+Pol M- and K-type Results

| Asteroid | Observation Date | UT | Total $t_{exp}$ (s) | Phase (deg) | Filter | $P_r$ | $\theta_r$ |
|---|---|---|---|---|---|---|---|
| 16 | 2019-08-30 | 05:22 | 2100 | 9.7 | *J* | −1.34% ± 0.10% | 92.2 ± 2.2 |
| 16 | 2021-02-03 | 04:23 | 1200 | 18.9 | *J* | −0.58% ± 0.10% | 89.4 ± 5.1 |
| 16 | 2021-02-03 | 04:32 | 1200 | 18.9 | *H* | −0.56% ± 0.10% | 92.7 ± 5.2 |
| 16 | 2023-01-07 | 13:30 | 160 | 15.1 | *J* | −1.08% ± 0.11% | 89.4 ± 2.8 |
| 16 | 2023-01-07 | 13:39 | 160 | 15.1 | *H* | −1.18% ± 0.20% | 85.2 ± 2.8 |
| 16 | 2023-05-16 | 07:25 | 160 | 2.5 | *J* | −0.86% ± 0.10% | 96.2 ± 3.7 |
| 16 | 2023-05-16 | 07:34 | 140 | 2.5 | *H* | −0.56% ± 0.10% | 83.0 ± 5.5 |
| 16 | 2024-05-19 | 11:14 | 160 | 20.6 | *J* | −0.35% ± 0.10% | 85.2 ± 8.6 |
| 16 | 2024-05-19 | 11:23 | 160 | 20.6 | *H* | −0.44% ± 0.10% | 85.0 ± 6.7 |
| 16 | 2024-07-22 | 06:00 | 160 | 6.4 | *J* | −1.29% ± 0.10% | 92.8 ± 2.3 |
| 16 | 2024-07-22 | 06:09 | 160 | 6.4 | *H* | −0.93% ± 0.10% | 82.0 ± 3.2 |
| 21 | 2025-03-01 | 09:13 | 165 | 6.1 | *J* | −1.34% ± 0.18% | 81.7 ± 3.4 |
| 21 | 2025-03-01 | 09:21 | 145 | 6.1 | *H* | −1.44% ± 0.17% | 86.1 ± 3.2 |
| 21 | 2025-03-02 | 09:26 | 160 | 6.5 | *J* | −1.49% ± 0.11% | 82.9 ± 2.1 |
| 21 | 2025-03-02 | 09:34 | 160 | 6.5 | *H* | −1.40% ± 0.11% | 83.1 ± 2.2 |
| 21 | 2025-04-12 | 03:29 | 160 | 18.4 | *J* | −0.66% ± 0.12% | 75.6 ± 4.5 |
| 21 | 2025-04-12 | 03:43 | 160 | 18.4 | *H* | −0.78% ± 0.12% | 94.8 ± 4.0 |
| 21 | 2025-05-28 | 04:04 | 320 | 20.7 | *J* | −0.57% ± 0.14% | 109.5 ± 8.6 |
| 21 | 2025-05-28 | 04:11 | 320 | 20.7 | *H* | −0.61% ± 0.15% | 101.8 ± 7.1 |
| 55 | 2025-03-02 | 09:16 | 160 | 13.9 | *H* | −1.10% ± 0.15% | 83.9 ± 2.8 |
| 89 | 2023-01-14 | 10:01 | 160 | 4.9 | *H* | −0.84% ± 0.10% | 95.1 ± 3.5 |
| 135 | 2025-03-02 | 08:29 | 960 | 10.3 | *J* | −1.24% ± 0.11% | 81.7 ± 2.4 |
| 135 | 2025-03-02 | 08:51 | 960 | 10.3 | *H* | −1.45% ± 0.11% | 89.5 ± 2.0 |
| 216 | 2023-01-14 | 03:23 | 160 | 26.5 | *J* | +0.72% ± 0.10% | 1.6 ± 4.2 |
| 216 | 2023-01-14 | 03:31 | 160 | 26.5 | *H* | +0.64% ± 0.10% | 176.1 ± 4.7 |
| 216 | 2024-01-29 | 08:10 | 160 | 9.4 | *J* | −1.16% ± 0.10% | 91.8 ± 2.8 |
| 216 | 2024-01-29 | 08:20 | 160 | 9.4 | *H* | −1.03% ± 0.10% | 88.6 ± 3.1 |
| 216 | 2024-05-19 | 03:57 | 160 | 19.1 | *J* | −0.65% ± 0.24% | 97.2 ± 10.0 |
| 216 | 2024-05-19 | 04:06 | 160 | 19.1 | *H* | −0.66% ± 0.13% | 120.9 ± 12.8 |
| 216 | 2025-05-28 | 04:41 | 160 | 11.4 | *J* | −0.85% ± 0.12% | 87.2 ± 3.7 |
| 216 | 2025-05-28 | 04:49 | 160 | 11.4 | *H* | −1.12% ± 0.14% | 88.3 ± 2.9 |
| 221 | 2021-11-08 | 09:18 | 2880 | 7.6 | *H* | −1.31% ± 0.10% | 87.0 ± 2.2 |
| 221 | 2021-11-08 | 09:29 | 2880 | 7.6 | *J* | −1.16% ± 0.10% | 88.5 ± 2.5 |
| 221 | 2022-12-01 | 10:22 | 960 | 16.8 | *H* | −1.31% ± 0.11% | 92.1 ± 2.3 |
| 221 | 2022-12-01 | 10:33 | 960 | 16.8 | *J* | −1.05% ± 0.11% | 84.0 ± 2.8 |
| 221 | 2023-01-07 | 09:27 | 960 | 9.6 | *J* | −1.12% ± 0.10% | 90.5 ± 2.7 |
| 221 | 2023-01-07 | 09:50 | 960 | 9.6 | *H* | −1.32% ± 0.11% | 90.5 ± 2.2 |
| 221 | 2024-01-29 | 13:08 | 960 | 17.4 | *J* | −0.89% ± 0.12% | 89.8 ± 3.5 |
| 221 | 2024-01-29 | 13:30 | 960 | 17.4 | *H* | −0.90% ± 0.16% | 87.7 ± 3.6 |
| 221 | 2024-05-19 | 08:49 | 160 | 12.8 | *J* | −1.30% ± 0.14% | 89.3 ± 3.4 |
| 221 | 2024-05-19 | 08:57 | 160 | 12.8 | *H* | −1.28% ± 0.13% | 86.9 ± 3.2 |
| 221 | 2025-05-28 | 09:31 | 320 | 16.4 | *J* | −1.08% ± 0.11% | 89.5 ± 2.9 |
| 221 | 2025-05-28 | 09:39 | 320 | 16.4 | *H* | −1.13% ± 0.11% | 88.5 ± 2.9 |
| 233 | 2023-07-26 | 09:40 | 160 | 22.6 | *J* | −0.32% ± 0.11% | 110.3 ± 9.6 |
| 233 | 2023-07-26 | 09:49 | 160 | 22.6 | *H* | −0.26% ± 0.10% | 73.7 ± 12.2 |
| 233 | 2023-08-26 | 07:12 | 160 | 14.4 | *J* | −1.48% ± 0.10% | 92.5 ± 2.1 |
| 233 | 2023-08-26 | 07:20 | 160 | 14.4 | *H* | −1.34% ± 0.10% | 87.4 ± 2.4 |
| 233 | 2025-03-02 | 07:42 | 960 | 15.9 | *J* | −1.22% ± 0.11% | 86.6 ± 2.4 |
| 233 | 2025-03-02 | 08:05 | 960 | 16.0 | *H* | −1.20% ± 0.11% | 93.1 ± 2.4 |

**Note.** The degree of polarization $P_r$ has been rotated so that positive values represent polarization perpendicular to the Sun-asteroid-telescope scattering plane at the time of the observations, and negative values represent polarization in this plane. $\theta_r$ is the measured angle of polarization after correcting for the observed $7\overset{\circ}{.}8$ systematic offset and rotated so that 0° is aligned with the vector perpendicular to the scattering plane.

indicate that the iron-sulfide troilite (FeS) in the objects we observed is generally finer-grained than the silicate and so is contributing less to the near-infrared polarimetric properties, yet still dominates the surface reflectance. We would then interpret Lutetia as having a comparable size distribution for the troilite and silicate components of its regolith in the size range probed by our observations.

It should be noted that the geometric albedo that R. Sultana et al. (2023a) determined for these mixtures ($p_V \sim 5\%$) is significantly lower than what is observed for M- and K-type asteroids. This may be due to the exclusive use of sub-$\mu$m materials used to build the aggregates tested, compared with real regoliths that would have a range of particle sizes. If the polarization effects are dominated by different components of

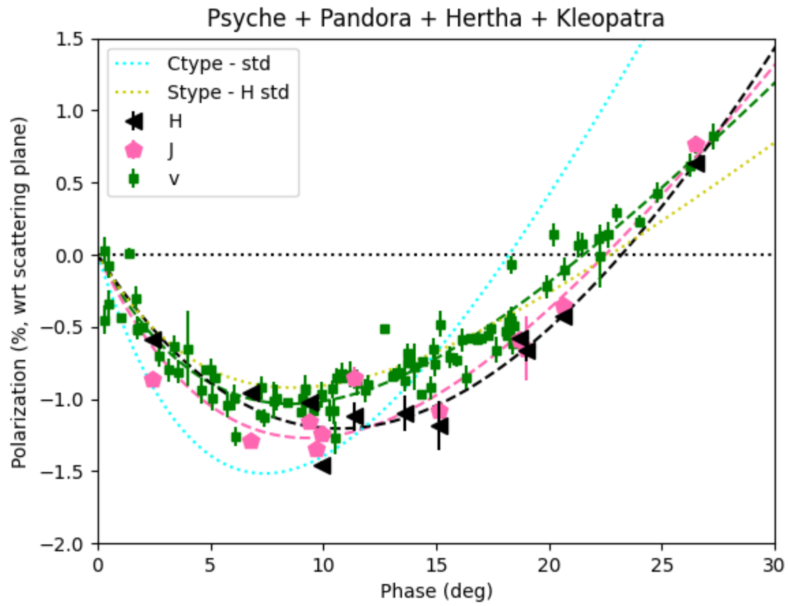


**Figure 1.** Polarimetric phase curves for M-type asteroids (16) Psyche, (55) Pandora, (135) Hertha, and (216) Kleopatra. *J*- and *H*-band observations were obtained using Palomar/WIRC+Pol, while the visible bands are from D. Lupishko (2022). Points show the measurements, while the lines are best-fit polarization phase curves based on theoretical scattering models. The light-blue and light-yellow lines show the best-fit curves to the NIR polarization-phase relationships for C-types at all wavelengths and S-complex objects at the *H* band (respectively, noted as "Ctype—std" and "Stype—H std") as derived by J. Masiero et al. (2022) for comparison.

**Table 2**
Polarization Phase Curve Fits

| Band | $P_{\min}$ (%) | $\alpha_{\min}$ (deg) | $h$ (%/deg) | $\alpha_0$ (deg) |
|---|---|---|---|---|
| **M-type** | | | | |
| *V* | $-1.03^{+0.01}_{-0.01}$ | $8.5^{+0.2}_{-0.2}$ | $0.13^{+0.01}_{-0.01}$ | $21.5^{+0.1}_{-0.1}$ |
| *J* | $-1.27^{+0.02}_{-0.02}$ | $9.3^{+0.5}_{-0.5}$ | $0.16^{+0.01}_{-0.01}$ | $22.5^{+0.2}_{-0.3}$ |
| *H* | $-1.21^{+0.04}_{-0.04}$ | $10.7^{+0.3}_{-0.4}$ | $0.18^{+0.01}_{-0.01}$ | $23.2^{+0.1}_{-0.1}$ |
| K-type | | | | |
| *V* | $-0.97^{+0.02}_{-0.02}$ | $8.9^{+0.3}_{-0.3}$ | $0.11^{+0.01}_{-0.01}$ | $22.8^{+0.3}_{-0.3}$ |
| *J* | $-1.30^{+0.02}_{-0.02}$ | $11.9^{+0.2}_{-0.2}$ | $0.20^{+0.01}_{-0.01}$ | $24.5^{+0.4}_{-0.3}$ |
| *H* | $-1.37^{+0.02}_{-0.02}$ | $11.7^{+0.2}_{-0.2}$ | $0.21^{+0.01}_{-0.01}$ | $24.2^{+0.1}_{-0.1}$ |
| M - and K-types fit jointly | | | | |
| *V* | $-1.01^{+0.01}_{-0.01}$ | $8.5^{+0.2}_{-0.1}$ | $0.12^{+0.01}_{-0.01}$ | $21.8^{+0.1}_{-0.1}$ |
| *J* | $-1.29^{+0.01}_{-0.01}$ | $10.9^{+0.2}_{-0.3}$ | $0.19^{+0.01}_{-0.01}$ | $23.3^{+0.1}_{-0.1}$ |
| *H* | $-1.29^{+0.02}_{-0.02}$ | $11.3^{+0.2}_{-0.1}$ | $0.20^{+0.01}_{-0.01}$ | $23.6^{+0.1}_{-0.1}$ |
| (21) Lutetia | | | | |
| *V* | $-1.34^{+0.02}_{-0.02}$ | $9.5^{+0.2}_{-0.3}$ | $0.15^{+0.01}_{-0.01}$ | $23.9^{+0.2}_{-0.3}$ |

**Note.** Parameters of the best-fit polarization phase curve: $P_{\min}$—the negative extrema of the curve; $\alpha_{\min}$—the phase angle where the curve reaches $P_{\min}$; $h$—the slope of the curve at the inversion angle; $\alpha_0$—the inversion angle of the curve (where the curve crosses $P = 0$). 16th and 84th percentile uncertainties, determined by fits to Monte Carlo simulations of the polarimetric measurements, are provided for each parameter.

the surface than those that produce the albedo effects, this could explain the discrepancy seen here.

The K-type taxonomic class was identified by S. J. Bus & R. Binzel (2002) as showing muted silicate-like absorption features and a less red slope. The canonical member of this class is (221) Eos, the largest object of a populous, moderate-albedo family in the outer main belt (J. Masiero et al. 2013). The asteroid (298) Baptistina has also been associated with the M, K, or Xk class, depending of the taxonomic scheme (V. Reddy et al. 2014; M. Mahlke et al. 2022) based on its moderate albedo and weak 1 and 2 $\mu$m absorption features, which is a good match for a mixture of silicate rich LL-chondrites and impact melted material. Baptistina and Eos also have very similar albedos at 3.4 $\mu$m (the WISE W1 band) of $p_{3.4\mu m} = 0.193 \pm 0.04$ and $p_{3.4\mu m} = 0.194 \pm 0.03$, respectively (J. Masiero et al. 2014; A. K. Mainzer et al. 2019). NEOWISE collected these 3.4 $\mu$m measurements simultaneously with the thermal emission measurements used to determine diameter, meaning that albedos determined in this way are subject to significantly fewer systematic uncertainties than visual albedos inferred from $H_V$ values. (The 3.4 $\mu$m albedos for our other targets discussed here are also in the moderate region between the bulk of C- and S-complex objects as fit by J. Masiero et al. (2014): (233) Asterope has $p_{3.4\mu m} = 0.14 \pm 0.02$, (75) Eurydike has $p_{3.4\mu m} = 0.19 \pm 0.01$, and (216) Kleopatra has $p_{3.4\mu m} = 0.23 \pm 0.02$.)

The spectrum of Baptistina has been shown to be a good match to the Chelyabinsk meteorite (V. Reddy et al. 2014). Chelyabinsk shows clear evidence of having undergone a catastrophic shocking process in its past, likely a massive collision between ∼100 km-scale asteroids resulting in a complete shattering of the parent body. This darkening process involves melting and migration of the troilite in the mineral matrix (T. Kohout et al. 2020), indicating that the parent body had experienced some level of heating prior to the impact. Troilite has a moderate albedo and featureless spectrum (D. Britt et al. 1992a), which would be expected to mute any silicate features of an intermixed surface material.

Atacama Large Millimeter/submillimeter Array (ALMA) observations of M-type objects (16) Psyche (K. de Kleer et al. 2021) and (22) Kalliope (K. de Kleer et al. 2024) at submillimeter wavelengths show that the surface materials of these bodies have a moderate emissivity that is consistent with metal in mineral phases such as sulfides or oxides. One

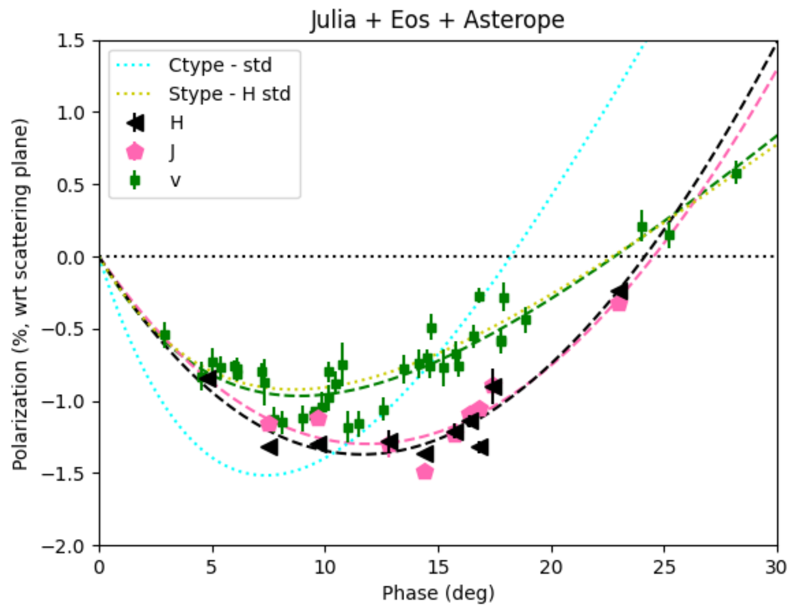


**Figure 2.** The same as Figure 1, showing polarimetric phase curves for K-type asteroids (89) Julia, (221) Eos, and (233) Asterope.

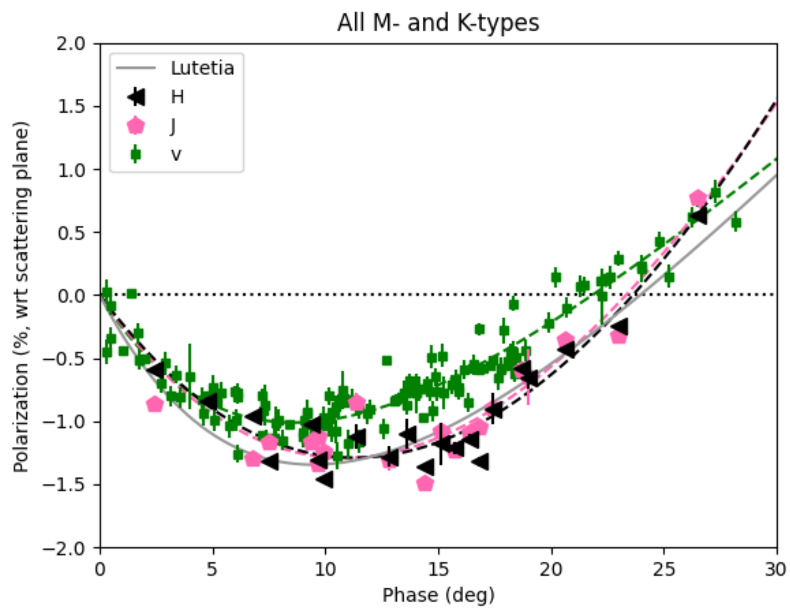


**Figure 3.** The same as Figure 1, showing the combined data for M- and K-types, the best fits to these data, with the best-fit curve to the (21) Lutetia *V*-band data overlaid.

complicating factor with these observations is the unexpectedly low polarization of the submillimeter emission, which these works interpret as large grains of pure metal (100 $\mu$m) in the surface material that scatter and depolarize the submillimeter emission. If these M-type objects have a surface dominated by troilite with significant pure metal inclusions within the surface layer, this would be consistent with the ALMA observations.

The polarimetric link we observe here suggests that, despite different spectral taxonomic classifications, the K- and M-type asteroids may in fact be mineralogically related and have undergone the same geophysical processes. Taxonomy determined from spectral observations is most strongly affected by the mineralogical absorption features from iron at 1 and 2 $\mu$m (S. J. Bus et al. 2002), while polarimetry is able to probe different properties of the mineral matrix like scattering element size, physical grain size, and index of refraction, which offer a more complete view of the composition of these objects (I. Belskaya et al. 2015).

We note that alternate taxonomic systems place all of the objects discussed here in similar regions of principal component space, even if the assigned taxonomic identifier is different. For example, F. E. DeMeo et al. (2009) classify these objects as Xk (Psyche, Asterope), K (Eos), Xe (Kleopatra), and Xc (Lutetia). The Tholen classification system (which included albedo) classifies Psyche, Lutetia, and Kleopatra as M-type, with Eos as an S-type and Asterope as a T-type. (298) Baptistina has an Xc taxonomy in the Bus

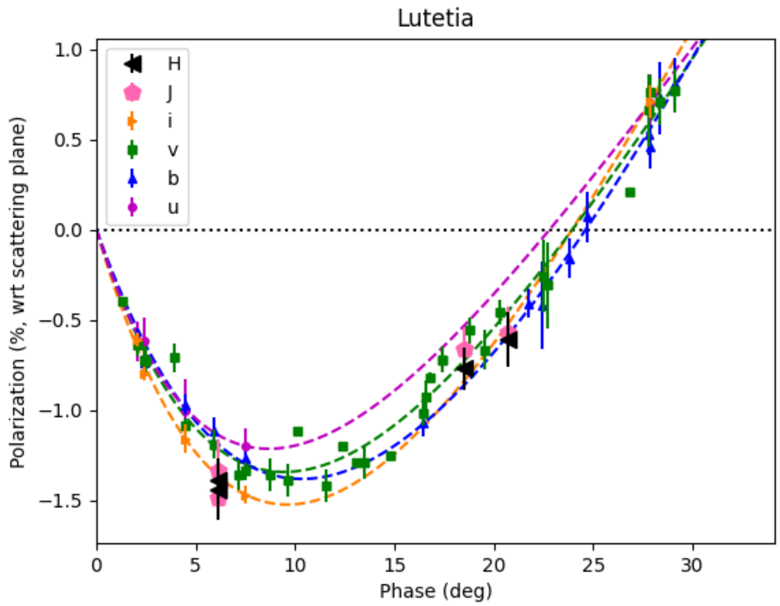


**Figure 4.** The same as Figure 1, showing polarimetric phase curves for M-type asteroid (21) Lutetia.

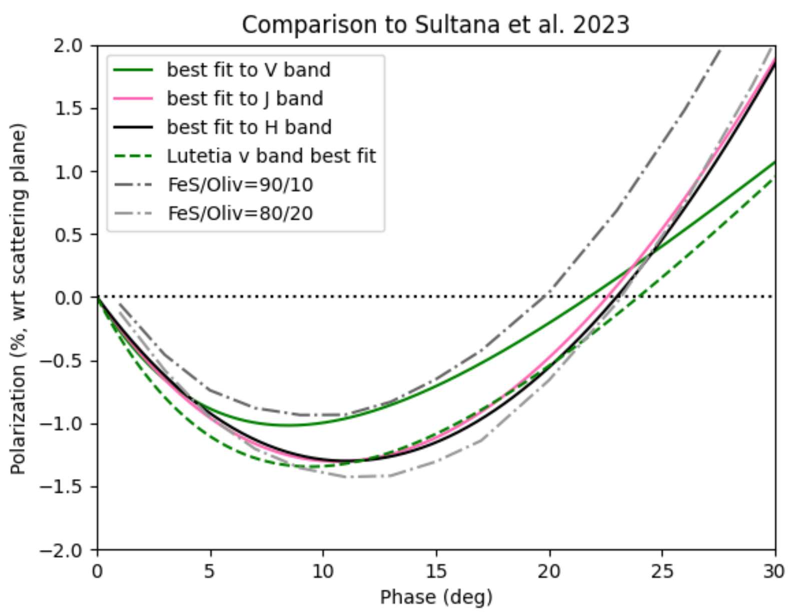


**Figure 5.** The best-fit *V*-, *J*-, and *H*-band curves shown in Figure 3 compared to laboratory measurements of troilite–olivine mixtures from R. Sultana et al. (2023b). FeS/Oliv = 90/10 is a mixture of 90% troilite and 10% olivine, while FeS/Oliv = 80/20 is an 80%/20% mixture. See R. Sultana et al. (2023a) for more details on the sample materials.

taxonomic system (D. Lazzaro et al. 2004), while M. Mahlke et al. (2022) place all our targets in their larger M complex. All these taxonomic systems support an interpretation of a compositional link and a continuum of spectral behavior.

T. Mothé-Diniz & J. M. Carvano (2005) proposed that the Eos asteroid family, which is one of the largest collections of K-type objects, is the remnant of a partially differentiated parent body. They show a notable similarity between the spectrum of (221) Eos and the anomalous, differentiated meteorite Divnoe. Further analysis by T. Mothé-Diniz et al. (2008) of 30 family members suggested a connection to the R-chondrites, a class of olivine-rich, metal-poor meteorites that have compositions that are consistent with partial differentiation. (Although it should be noted that conversely, B. E. Clark et al. 2009 associate K-type asteroids with CO/CV/CK carbonaceous chondrites.)

P. Vernazza et al. (2011) compared the spectra of Lutetia obtained from Rosetta to RELAB meteorite samples, finding that the enstatite chondrites are the closest match over the optical to near-infrared range. These results point to a probable formation region for Lutetia in the terrestrial planet region, the same location proposed as a probable source of the differentiated (or partially differentiated) parents of the iron meteorites (W. F. Bottke et al. 2006).

Recently, K. McFadden et al. (2025) performed a reanalysis of the NEOWISE using the multiepoch observations to constrain 3.4 $\mu$m (W1) albedos for a larger number of objects than were possible for J. Masiero et al. (2014). Using these fits, we can identify the population of objects with V- and W1 albedos consistent with the objects discussed here. These fits show that (21) Lutetia has $p_{\mathrm{W1}} = 0.24 \pm 0.04$, further supporting the polarimetric link proposed here. Other objects with moderate V albedos and W1 albedos include (51) Nemausa, (97) Klotho, (201) Penelope, and (339) Dorothea, all of which would benefit from future investigation. We have obtained observations of Klotho at a single phase angle (see Table A1), which show a significantly deeper polarization than would be expected from the other M-type objects investigated here. This may be an outlier or indicate a difference in surface properties, making this object particularly interesting for obtaining more observational data.

Taken together, these measurements may then help us settle the "missing mantle" problem: instead of basaltic material from a fully melted object like Vesta, the detritus from the collisions that exposed the M-type metal-rich asteroids and the iron meteorites may be the population of K-type objects currently in our catalogs. This is consistent with the link between T-type asteroids and troilite proposed by D. Britt et al. (1992b; two of the three T-type objects from that study showing the best link have alternate taxonomic classifications of M/K classification). Our best interpretation of these objects would be targets that are rich in troilite, with K-type objects having been closer to the surface of the parent body than the present-day M-types. The spectral features of troilite are consistent with the moderate optical and near-infrared albedos observed for K- and M-type asteroids.

## 5. Implications for Psyche

The NASA Psyche mission launched in 2023 and will be rendezvousing with the asteroid (16) Psyche in 2029 to perform a detailed analysis of this metal-rich target (S. D. Dibb et al. 2024). The spacecraft carries a spectrophotometer, a gamma-ray and neutron spectrometer, and a magnetometer, which it will use to map the topography and measure the internal gravity and surface composition of the asteroid. Based on the link that we present here between the K- and M-type objects, we would anticipate that the results from Psyche will generally show a surface that is a mixture of shocked silicate materials in a surface dominated by troilite or other iron-rich minerals, rather than a pure metallic surface. This would be consistent with the observations presented by J. Sanchez et al. (2017) and D. Cantillo et al. (2021) showing that spectral observations of (16) Psyche indicate a surface that is composed of primarily an iron-rich material with ∼10%–15% of pyroxene and chondritic materials, as well as the ALMA results shown by K. de Kleer et al. (2021).

Troilite is commonly found intermixed in iron meteorites, though it is significantly weaker than iron-nickel, and so would be expected to dominate the regolith of a body that has undergone significant gardening from background impacts over gigayear timescales. It has a higher density than the silicates commonly found in meteorites, and so would contribute to the overall high bulk density of (16) Psyche. As troilite is nonmagnetic, it would not be expected to contribute to any surface magnetic fields that could be detected by the Psyche mission.

## 6. Conclusions

We present new near-infrared polarimetric observations of M- and K-type asteroids. Our observations show changes from visible to NIR wavelengths that are consistent between these two classes, which indicate a mineralogical link between these populations. Further observations of more members of these populations and more complete near-infrared phase curves for the object shown here will help improve this link. The associations of these two populations with extreme collisions in the early solar system connect the evolution of these bodies as well as their composition. Taken together, these features paint a compelling story for small body evolution, with iron meteorites and M-type asteroids representing the interiors of partially differentiated, troilite-rich, collisionally disrupted protoplanets, and K-type bodies tracing the material that originated closer to the surface that was dispersed during these ancient collisions.

## Acknowledgments

We thank the referees for the helpful comments that improved this paper. J.R.M. thanks Dan Britt, Olivier Poch, and Michele Bannister for very helpful discussions in interpreting these results, and the staff of Palomar Observatory for all their assistance over the years in collecting these observations. Based on observations obtained at the Hale Telescope, Palomar Observatory as part of a continuing collaboration between the California Institute of Technology, NASA/JPL, Yale University, and the National Astronomical Observatories of China. This research made use of Photutils, an Astropy (http://www.astropy.org) package for detection and photometry of astronomical sources (L. Bradley et al. 2019). This work made use of Astropy: a community-developed core Python package and an ecosystem of tools and resources for astronomy (Astropy Collaboration et al. 2013, 2018, 2022). This publication makes use of data products from the Wide-field Infrared Survey Explorer, which is a joint project of the University of California, Los Angeles, and the Jet Propulsion Laboratory/California Institute of Technology, funded by the National Aeronautics and Space Administration. This publication also makes use of data products from NEOWISE, which is a joint project of University of California, Los Angeles and the Jet Propulsion Laboratory/California Institute of Technology, funded by the Planetary Science Division of the National Aeronautics and Space Administration. This research has made use of data and services provided by the International Astronomical Union's Minor Planet Center. This research has made use of NASA's Astrophysics Data System

## Appendix
## Incidental Observations

Table A1 presents incidental observations of other main belt asteroids obtained with WIRC+Pol over the course of our survey. Observations originally presented in J. Masiero et al. (2022) are revised here with corrected $\theta$ angles of polarization and polarization uncertainties. Observations presented in J. Masiero et al. (2023) are unchanged and so not included in this table. Two notable objects from our sample are shown in Figures A1 and A2: T-type object (72) Feronia, which shows the deepest $P_{\mathrm{min}}$ of any object observed, and S/L-type object (12) Victoria, which shows a continuation to the near-infrared of the shift in polarization-phase curve observed by I. N. Belskaya et al. (2009).

**Table A1**
WIRC+Pol Incidental Main Belt Observations

| Asteroid | Observation Date | UT | Total $t_{exp}$ (s) | Phase (deg) | Filter | $P_r$ | $\theta_r$ |
|---|---|---|---|---|---|---|---|
| 1 | 2021-09-04 | 10:57 | 320 | 21.0 | *J* | +0.89% ± 0.10% | 179.9 ± 3.3 |
| 1 | 2021-09-04 | 11:02 | 320 | 21.0 | *H* | +0.88% ± 0.10% | 7.7 ± 3.3 |
| 1 | 2021-11-08 | 10:39 | 32 | 8.2 | *H* | −1.59% ± 0.10% | 94.4 ± 1.8 |
| 1 | 2021-11-08 | 10:44 | 32 | 8.2 | *J* | −1.78% ± 0.10% | 89.4 ± 1.7 |
| 1 | 2022-04-02 | 04:51 | 160 | 19.3 | *J* | +0.52% ± 0.10% | 3.6 ± 5.7 |
| 1 | 2023-01-07 | 10:26 | 32 | 22.1 | *J* | +1.35% ± 0.10% | 179.9 ± 2.2 |
| 1 | 2023-01-07 | 10:33 | 32 | 22.1 | *H* | +1.26% ± 0.10% | 0.2 ± 2.3 |
| 1 | 2023-05-16 | 05:39 | 32 | 20.1 | *J* | +0.38% ± 0.10% | 7.3 ± 7.8 |
| 1 | 2023-05-16 | 05:46 | 32 | 20.1 | *H* | +0.87% ± 0.10% | 179.6 ± 3.4 |
| 1 | 2023-07-26 | 04:01 | 160 | 20.9 | *J* | +0.81% ± 0.10% | 179.7 ± 3.6 |
| 1 | 2023-07-26 | 04:10 | 160 | 20.9 | *H* | +0.93% ± 0.10% | 2.8 ± 3.1 |
| 1 | 2024-05-19 | 11:33 | 32 | 16.3 | *J* | −0.51% ± 0.10% | 87.6 ± 5.7 |
| 1 | 2024-05-19 | 11:39 | 32 | 16.3 | *H* | −0.35% ± 0.10% | 76.7 ± 8.5 |
| 2 | 2019-03-17 | 09:32 | 505 | 13.9 | *J* | −1.01% ± 0.10% | 94.8 ± 2.9 |
| 2 | 2019-03-17 | 10:08 | 510 | 13.9 | *H* | −0.80% ± 0.10% | 98.3 ± 3.7 |
| 2 | 2021-05-30 | 11:19 | 480 | 17.4 | *H* | −0.24% ± 0.10% | 99.1 ± 12.1 |
| 2 | 2021-05-30 | 11:24 | 480 | 17.4 | *J* | −0.30% ± 0.10% | 87.5 ± 9.8 |
| 2 | 2021-06-26 | 10:44 | 32 | 18.0 | *H* | −0.17% ± 0.10% | 65.7 ± 18.3 |
| 2 | 2021-06-26 | 10:48 | 32 | 18.0 | *J* | −0.16% ± 0.10% | 67.5 ± 20.2 |
| 2 | 2021-09-04 | 07:32 | 160 | 3.2 | *H* | −1.35% ± 0.10% | 90.0 ± 2.2 |
| 2 | 2021-09-04 | 07:37 | 160 | 3.2 | *J* | −1.27% ± 0.10% | 91.9 ± 2.3 |
| 2 | 2021-11-08 | 04:21 | 160 | 17.4 | *H* | −0.26% ± 0.10% | 80.2 ± 11.6 |
| 2 | 2021-11-08 | 04:26 | 160 | 17.4 | *J* | −0.11% ± 0.10% | 87.8 ± 25.8 |
| 2 | 2022-10-15 | 12:10 | 24 | 26.0 | *H* | +2.00% ± 0.10% | 1.3 ± 1.5 |
| 2 | 2024-01-29 | 12:19 | 160 | 20.5 | *J* | +0.50% ± 0.10% | 4.0 ± 5.9 |
| 2 | 2024-01-29 | 12:28 | 160 | 20.5 | *H* | +0.62% ± 0.10% | 2.5 ± 4.7 |
| 2 | 2024-05-19 | 09:45 | 160 | 14.5 | *J* | −0.72% ± 0.10% | 87.0 ± 4.1 |
| 2 | 2024-05-19 | 09:54 | 160 | 14.5 | *H* | −0.86% ± 0.10% | 88.8 ± 3.4 |
| 2 | 2025-04-12 | 11:54 | 160 | 16.0 | *J* | −0.73% ± 0.10% | 85.7 ± 4.1 |
| 2 | 2025-04-12 | 12:03 | 160 | 16.0 | *H* | −0.62% ± 0.10% | 88.8 ± 4.7 |
| 2 | 2025-05-28 | 09:02 | 160 | 17.0 | *J* | −0.42% ± 0.10% | 88.1 ± 7.1 |
| 2 | 2025-05-28 | 09:10 | 160 | 17.0 | *H* | −0.49% ± 0.10% | 80.6 ± 6.0 |
| 3 | 2021-05-30 | 07:53 | 640 | 6.2 | *J* | −0.72% ± 0.10% | 88.9 ± 4.1 |
| 3 | 2021-05-30 | 07:57 | 645 | 6.2 | *H* | −0.95% ± 0.10% | 89.6 ± 3.1 |
| 3 | 2021-06-26 | 07:16 | 240 | 8.6 | *H* | −0.75% ± 0.10% | 87.4 ± 3.9 |
| 3 | 2021-06-26 | 07:21 | 240 | 8.6 | *J* | −0.86% ± 0.10% | 95.6 ± 3.4 |
| 3 | 2021-09-04 | 03:56 | 120 | 18.4 | *H* | −0.45% ± 0.11% | 100.8 ± 6.5 |
| 3 | 2021-09-04 | 03:59 | 120 | 18.4 | *J* | −0.47% ± 0.11% | 83.6 ± 6.3 |
| 3 | 2022-05-31 | 11:28 | 160 | 23.0 | *H* | +0.17% ± 0.10% | 164.7 ± 17.4 |
| 3 | 2022-05-31 | 11:32 | 160 | 23.0 | *J* | +0.26% ± 0.10% | 9.3 ± 11.5 |
| 3 | 2022-07-11 | 09:31 | 160 | 21.2 | *H* | −0.16% ± 0.10% | 76.5 ± 18.5 |
| 3 | 2022-07-11 | 09:35 | 160 | 21.2 | *J* | +0.03% ± 0.10% | 172.9 ± 86.3 |
| 3 | 2022-10-15 | 04:57 | 160 | 18.1 | *H* | −0.41% ± 0.10% | 89.1 ± 7.0 |
| 3 | 2022-10-15 | 05:02 | 160 | 18.1 | *J* | −0.33% ± 0.10% | 93.2 ± 9.0 |
| 3 | 2023-01-07 | 03:28 | 160 | 26.9 | *J* | +0.70% ± 0.10% | 4.8 ± 4.2 |
| 3 | 2023-01-07 | 03:38 | 160 | 26.9 | *H* | +0.39% ± 0.10% | 179.8 ± 7.5 |
| 3 | 2024-01-29 | 09:19 | 160 | 14.8 | *J* | −0.44% ± 0.10% | 85.5 ± 6.7 |
| 3 | 2024-01-29 | 09:28 | 160 | 14.8 | *H* | −0.70% ± 0.10% | 83.0 ± 4.2 |
| 4 | 2019-08-30 | 10:13 | 2380 | 23.3 | *J* | −0.09% ± 0.10% | 55.6 ± 32.9 |
| 4 | 2021-02-03 | 11:38 | 40 | 14.3 | *H* | −0.65% ± 0.11% | 89.2 ± 4.5 |
| 4 | 2021-02-03 | 11:43 | 41 | 14.3 | *J* | −0.31% ± 0.11% | 93.6 ± 9.6 |
| 4 | 2021-05-30 | 06:22 | 64 | 26.6 | *J* | +0.15% ± 0.10% | 11.0 ± 19.9 |
| 4 | 2021-05-30 | 06:26 | 64 | 26.6 | *H* | +0.25% ± 0.10% | 3.6 ± 11.8 |
| 4 | 2021-06-26 | 04:15 | 48 | 26.2 | *H* | +0.13% ± 0.10% | 166.8 ± 22.5 |
| 4 | 2021-06-26 | 04:19 | 48 | 26.2 | *J* | +0.18% ± 0.10% | 17.1 ± 16.0 |
| 4 | 2022-07-11 | 10:00 | 64 | 19.6 | *J* | −0.22% ± 0.11% | 120.8 ± 13.3 |
| 4 | 2022-07-11 | 10:03 | 64 | 19.6 | *H* | −0.36% ± 0.10% | 73.6 ± 8.3 |
| 4 | 2022-10-15 | 04:19 | 32 | 21.4 | *H* | −0.23% ± 0.10% | 100.5 ± 12.9 |
| 4 | 2022-10-15 | 04:23 | 32 | 21.4 | *J* | −0.12% ± 0.10% | 97.3 ± 24.2 |
| 4 | 2022-12-01 | 03:01 | 32 | 24.3 | *H* | −0.03% ± 0.10% | 93.9 ± 109.0 |
| 4 | 2022-12-01 | 03:04 | 32 | 24.3 | *J* | +0.08% ± 0.10% | 10.0 ± 35.7 |
| 4 | 2023-01-14 | 02:20 | 32 | 19.6 | *J* | −0.07% ± 0.10% | 67.6 ± 45.8 |
| 4 | 2023-01-14 | 02:27 | 32 | 19.6 | *H* | −0.20% ± 0.10% | 89.5 ± 14.5 |

**Table A1**
(Continued)

| Asteroid | Observation Date | UT | Total $t_{\exp}$ (s) | Phase (deg) | Filter | $P_r$ | $\theta_r$ |
|---|---|---|---|---|---|---|---|
| 6 | 2023-01-14 | 09:02 | 160 | 6.7 | $J$ | −0.79% ± 0.11% | 94.5 ± 4.1 |
| 6 | 2023-01-14 | 09:11 | 160 | 6.7 | $H$ | −0.66% ± 0.12% | 85.9 ± 5.6 |
| 6 | 2024-01-29 | 11:57 | 160 | 19.7 | $J$ | −0.34% ± 0.11% | 83.9 ± 8.6 |
| 6 | 2024-01-29 | 12:07 | 160 | 19.7 | $H$ | −0.57% ± 0.10% | 92.2 ± 5.1 |
| 7 | 2021-09-04 | 11:45 | 480 | 30.5 | $H$ | +0.71% ± 0.10% | 178.4 ± 4.2 |
| 7 | 2021-09-04 | 11:49 | 480 | 30.5 | $J$ | +0.81% ± 0.10% | 179.7 ± 3.7 |
| 7 | 2021-11-08 | 12:32 | 160 | 29.1 | $H$ | +0.62% ± 0.10% | 1.2 ± 4.7 |
| 7 | 2021-11-08 | 12:37 | 160 | 29.1 | $J$ | +0.72% ± 0.11% | 13.1 ± 4.1 |
| 7 | 2022-04-02 | 05:48 | 160 | 25.5 | $H$ | +0.22% ± 0.10% | 10.9 ± 13.5 |
| 7 | 2022-04-02 | 05:53 | 160 | 25.5 | $J$ | +0.18% ± 0.10% | 170.2 ± 16.8 |
| 7 | 2023-01-07 | 13:10 | 160 | 18.7 | $J$ | −0.39% ± 0.10% | 78.9 ± 7.6 |
| 7 | 2023-01-07 | 13:19 | 160 | 18.7 | $H$ | −0.58% ± 0.10% | 89.0 ± 5.0 |
| 7 | 2023-05-16 | 07:05 | 160 | 6.6 | $J$ | −1.26% ± 0.12% | 88.2 ± 2.5 |
| 7 | 2023-05-16 | 07:14 | 160 | 6.6 | $H$ | −0.96% ± 0.14% | 94.0 ± 3.1 |
| 10 | 2022-04-02 | 09:12 | 160 | 10.6 | $H$ | −1.19% ± 0.10% | 88.1 ± 2.5 |
| 10 | 2022-04-02 | 09:16 | 160 | 10.6 | $J$ | −0.99% ± 0.10% | 88.9 ± 3.0 |
| 10 | 2022-05-31 | 04:22 | 160 | 12.4 | $H$ | −0.92% ± 0.10% | 91.7 ± 3.2 |
| 10 | 2022-05-31 | 04:27 | 160 | 12.4 | $J$ | −0.89% ± 0.10% | 93.5 ± 3.3 |
| 10 | 2022-07-11 | 04:22 | 160 | 20.5 | $H$ | +0.82% ± 0.10% | 5.4 ± 3.6 |
| 10 | 2022-07-11 | 04:26 | 160 | 20.5 | $J$ | +0.83% ± 0.11% | 0.4 ± 3.6 |
| 10 | 2023-07-26 | 07:49 | 160 | 5.8 | $J$ | −1.45% ± 0.10% | 94.1 ± 2.1 |
| 10 | 2023-07-26 | 07:57 | 160 | 5.8 | $H$ | −0.98% ± 0.10% | 89.0 ± 3.0 |
| 10 | 2023-08-26 | 05:25 | 160 | 6.0 | $J$ | −1.43% ± 0.10% | 87.0 ± 2.1 |
| 10 | 2023-08-26 | 05:33 | 160 | 6.0 | $H$ | −1.08% ± 0.10% | 93.1 ± 2.7 |
| 10 | 2024-10-07 | 06:12 | 160 | 5.3 | $J$ | −1.30% ± 0.10% | 86.6 ± 2.3 |
| 10 | 2024-10-07 | 06:20 | 160 | 5.2 | $H$ | −1.23% ± 0.10% | 84.7 ± 2.4 |
| 12 | 2022-12-01 | 12:53 | 160 | 13.6 | $H$ | −1.05% ± 0.11% | 88.0 ± 2.8 |
| 12 | 2022-12-01 | 12:58 | 160 | 13.5 | $J$ | −1.02% ± 0.11% | 88.4 ± 2.9 |
| 12 | 2023-01-07 | 08:13 | 160 | 3.9 | $J$ | −0.50% ± 0.10% | 90.6 ± 5.9 |
| 12 | 2023-01-07 | 08:22 | 160 | 3.9 | $H$ | −0.71% ± 0.10% | 86.1 ± 4.2 |
| 12 | 2024-01-29 | 10:49 | 160 | 21.1 | $J$ | −0.75% ± 0.18% | 79.2 ± 4.6 |
| 12 | 2024-01-29 | 10:59 | 160 | 21.1 | $H$ | −0.97% ± 0.12% | 84.2 ± 3.2 |
| 12 | 2024-05-19 | 06:54 | 160 | 21.0 | $J$ | −0.55% ± 0.10% | 89.8 ± 5.3 |
| 12 | 2024-05-19 | 07:02 | 160 | 21.0 | $H$ | −0.81% ± 0.10% | 89.7 ± 3.6 |
| 15 | 2019-08-30 | 07:46 | 1400 | 9.5 | $J$ | −0.99% ± 0.10% | 91.6 ± 3.0 |
| 15 | 2021-02-03 | 05:47 | 400 | 6.1 | $J$ | −0.91% ± 0.10% | 91.3 ± 3.2 |
| 15 | 2021-02-03 | 05:53 | 400 | 6.1 | $H$ | −0.80% ± 0.10% | 94.9 ± 3.6 |
| 20 | 2021-11-08 | 12:01 | 320 | 28.7 | $J$ | +0.72% ± 0.10% | 175.8 ± 4.1 |
| 20 | 2021-11-08 | 12:06 | 320 | 28.7 | $H$ | +0.77% ± 0.10% | 179.8 ± 3.8 |
| 20 | 2022-04-02 | 07:00 | 160 | 23.9 | $H$ | +0.25% ± 0.10% | 2.8 ± 11.5 |
| 20 | 2022-04-02 | 07:05 | 160 | 23.9 | $J$ | +0.22% ± 0.10% | 167.7 ± 13.1 |
| 20 | 2023-07-26 | 06:10 | 160 | 15.2 | $J$ | −0.41% ± 0.10% | 91.3 ± 7.2 |
| 20 | 2023-07-26 | 06:19 | 160 | 15.2 | $H$ | −0.59% ± 0.10% | 87.9 ± 4.9 |
| 20 | 2023-08-26 | 03:23 | 160 | 20.7 | $J$ | −0.13% ± 0.11% | 72.4 ± 22.6 |
| 20 | 2023-08-26 | 03:33 | 160 | 20.7 | $H$ | −0.24% ± 0.10% | 118.4 ± 12.7 |
| 20 | 2024-10-07 | 06:33 | 320 | 3.9 | $H$ | −0.64% ± 0.10% | 86.2 ± 4.6 |
| 25 | 2021-11-08 | 06:04 | 160 | 11.0 | $H$ | −0.48% ± 0.10% | 78.9 ± 6.1 |
| 25 | 2021-11-08 | 06:08 | 160 | 11.0 | $J$ | −0.69% ± 0.10% | 87.3 ± 4.3 |
| 27 | 2023-01-14 | 04:30 | 160 | 27.6 | $J$ | +0.43% ± 0.10% | 16.4 ± 6.8 |
| 27 | 2023-01-14 | 04:38 | 160 | 27.6 | $H$ | +0.34% ± 0.10% | 11.5 ± 8.6 |
| 27 | 2024-01-29 | 12:39 | 160 | 23.7 | $J$ | +0.13% ± 0.10% | 28.6 ± 23.6 |
| 27 | 2024-01-29 | 12:49 | 160 | 23.7 | $H$ | +0.33% ± 0.11% | 3.9 ± 9.2 |
| 30 | 2023-01-14 | 04:50 | 160 | 21.4 | $J$ | −0.17% ± 0.10% | 74.4 ± 17.5 |
| 30 | 2023-01-14 | 04:59 | 160 | 21.4 | $H$ | −0.31% ± 0.10% | 85.6 ± 9.3 |
| 31 | 2022-10-15 | 05:35 | 160 | 2.7 | $H$ | −0.58% ± 0.10% | 101.4 ± 5.0 |
| 31 | 2022-10-15 | 05:40 | 160 | 2.7 | $J$ | −0.75% ± 0.10% | 93.2 ± 4.0 |
| 31 | 2022-12-01 | 05:59 | 160 | 17.4 | $H$ | −0.35% ± 0.10% | 84.9 ± 8.9 |
| 31 | 2022-12-01 | 06:04 | 160 | 17.4 | $J$ | −0.57% ± 0.10% | 81.8 ± 5.3 |
| 31 | 2023-01-07 | 04:34 | 160 | 21.6 | $H$ | +0.39% ± 0.10% | 179.6 ± 8.1 |
| 31 | 2023-01-07 | 04:43 | 160 | 21.6 | $J$ | +0.60% ± 0.10% | 179.0 ± 5.3 |
| 31 | 2024-01-29 | 10:07 | 160 | 14.8 | $J$ | −1.05% ± 0.11% | 87.8 ± 3.0 |
| 31 | 2024-01-29 | 10:16 | 160 | 14.8 | $H$ | −0.71% ± 0.11% | 89.0 ± 4.6 |
| 31 | 2024-05-19 | 07:12 | 160 | 20.8 | $H$ | +0.24% ± 0.12% | 3.2 ± 13.3 |

**Table A1**
(Continued)

| Asteroid | Observation Date | UT | Total $t_{exp}$ (s) | Phase (deg) | Filter | $P_r$ | $\theta_r$ |
|---|---|---|---|---|---|---|---|
| 31 | 2024-05-19 | 07:20 | 160 | 20.8 | *J* | +0.47% ± 0.11% | 4.6 ± 6.7 |
| 41 | 2022-04-02 | 11:57 | 160 | 27.5 | *H* | +2.49% ± 0.10% | 4.5 ± 1.2 |
| 41 | 2022-04-02 | 12:01 | 160 | 27.5 | *J* | +2.85% ± 0.10% | 1.3 ± 1.0 |
| 41 | 2022-05-31 | 09:49 | 160 | 14.3 | *H* | −1.66% ± 0.10% | 92.9 ± 1.8 |
| 41 | 2022-05-31 | 09:54 | 160 | 14.3 | *J* | −1.46% ± 0.10% | 93.4 ± 2.0 |
| 41 | 2022-07-11 | 07:22 | 160 | 19.3 | *H* | −0.07% ± 0.10% | 111.8 ± 40.7 |
| 41 | 2022-07-11 | 07:27 | 160 | 19.3 | *J* | −0.17% ± 0.10% | 79.3 ± 17.5 |
| 41 | 2023-07-26 | 10:07 | 960 | 17.9 | *J* | −0.82% ± 0.10% | 91.4 ± 3.6 |
| 41 | 2023-07-26 | 10:30 | 960 | 17.9 | *H* | −0.56% ± 0.10% | 76.0 ± 5.4 |
| 41 | 2023-08-26 | 07:38 | 960 | 12.2 | *J* | −1.81% ± 0.10% | 89.8 ± 1.6 |
| 41 | 2023-08-26 | 08:00 | 960 | 12.2 | *H* | −1.40% ± 0.10% | 86.8 ± 2.1 |
| 44 | 2021-11-08 | 11:28 | 160 | 16.7 | *H* | −0.18% ± 0.10% | 53.2 ± 16.5 |
| 44 | 2021-11-08 | 11:33 | 160 | 16.7 | *J* | −0.22% ± 0.10% | 69.9 ± 13.7 |
| 44 | 2022-04-02 | 05:29 | 160 | 28.2 | *H* | +0.35% ± 0.10% | 11.3 ± 8.4 |
| 44 | 2022-04-02 | 05:33 | 160 | 28.2 | *J* | +0.50% ± 0.10% | 176.1 ± 5.9 |
| 44 | 2023-01-07 | 13:49 | 160 | 20.6 | *J* | +0.38% ± 0.12% | 39.6 ± 12.5 |
| 44 | 2023-01-07 | 13:58 | 160 | 20.6 | *H* | +0.05% ± 0.10% | 20.2 ± 67.6 |
| 44 | 2023-05-16 | 07:55 | 160 | 3.6 | *H* | −0.44% ± 0.10% | 74.7 ± 7.0 |
| 46 | 2022-10-15 | 05:55 | 160 | 6.2 | *H* | −1.45% ± 0.10% | 90.9 ± 2.0 |
| 46 | 2022-10-15 | 05:59 | 160 | 6.2 | *J* | −1.82% ± 0.10% | 89.0 ± 1.6 |
| 46 | 2022-12-01 | 06:12 | 80 | 17.6 | *J* | −0.59% ± 0.11% | 102.3 ± 5.1 |
| 46 | 2023-01-07 | 05:00 | 960 | 25.1 | *J* | +2.69% ± 0.10% | 1.5 ± 1.1 |
| 46 | 2023-01-07 | 05:23 | 960 | 25.1 | *H* | +2.05% ± 0.10% | 0.7 ± 1.5 |
| 46 | 2024-01-29 | 08:36 | 960 | 9.1 | *J* | −1.17% ± 0.11% | 102.1 ± 2.9 |
| 46 | 2024-01-29 | 09:00 | 960 | 9.1 | *H* | −1.80% ± 0.14% | 88.0 ± 1.9 |
| 51 | 2022-05-31 | 07:50 | 160 | 17.6 | *H* | −0.55% ± 0.11% | 75.4 ± 5.3 |
| 51 | 2022-05-31 | 07:54 | 160 | 17.6 | *J* | −0.83% ± 0.10% | 81.6 ± 3.6 |
| 51 | 2022-07-11 | 06:14 | 160 | 25.7 | *H* | +1.67% ± 0.11% | 179.9 ± 1.8 |
| 51 | 2022-07-11 | 06:18 | 160 | 25.7 | *J* | +1.51% ± 0.11% | 179.9 ± 2.0 |
| 51 | 2023-07-26 | 09:02 | 160 | 19.2 | *J* | −0.47% ± 0.11% | 93.1 ± 6.8 |
| 51 | 2023-07-26 | 09:11 | 160 | 19.2 | *H* | −0.09% ± 0.10% | 73.5 ± 34.0 |
| 51 | 2023-08-26 | 06:34 | 160 | 8.4 | *J* | −1.99% ± 0.10% | 92.2 ± 1.5 |
| 51 | 2023-08-26 | 06:42 | 160 | 8.4 | *H* | −1.72% ± 0.10% | 84.7 ± 1.7 |
| 64 | 2023-01-14 | 06:20 | 160 | 5.5 | *J* | −0.45% ± 0.10% | 93.0 ± 6.5 |
| 64 | 2023-01-14 | 06:29 | 160 | 5.5 | *H* | −0.40% ± 0.10% | 91.9 ± 7.4 |
| 72 | 2022-07-11 | 07:02 | 160 | 6.3 | *H* | −2.61% ± 0.11% | 90.5 ± 1.1 |
| 72 | 2022-07-11 | 07:07 | 160 | 6.3 | *J* | −1.78% ± 0.11% | 89.0 ± 1.7 |
| 72 | 2022-10-15 | 03:34 | 960 | 29.7 | *H* | +2.22% ± 0.12% | 3.2 ± 1.4 |
| 72 | 2022-10-15 | 03:45 | 960 | 29.7 | *J* | +2.07% ± 0.11% | 0.1 ± 1.4 |
| 72 | 2022-12-01 | 02:29 | 960 | 27.0 | *H* | +1.31% ± 0.11% | 7.4 ± 2.3 |
| 72 | 2022-12-01 | 02:40 | 960 | 27.0 | *J* | +1.04% ± 0.11% | 1.5 ± 2.9 |
| 72 | 2023-08-26 | 11:49 | 1920 | 22.4 | *J* | −0.46% ± 0.13% | 56.1 ± 14.2 |
| 72 | 2023-08-26 | 12:12 | 1920 | 22.4 | *H* | +0.26% ± 0.12% | 11.9 ± 11.5 |
| 72 | 2024-01-29 | 06:52 | 960 | 13.5 | *J* | −2.21% ± 0.10% | 89.0 ± 1.3 |
| 72 | 2024-01-29 | 07:15 | 960 | 13.5 | *H* | −1.62% ± 0.11% | 91.4 ± 1.8 |
| 72 | 2025-04-12 | 08:20 | 160 | 8.0 | *J* | −2.04% ± 0.11% | 86.2 ± 1.5 |
| 72 | 2025-04-12 | 08:29 | 160 | 8.0 | *H* | −2.43% ± 0.11% | 88.3 ± 1.2 |
| 72 | 2025-05-28 | 05:31 | 140 | 15.9 | *J* | −1.85% ± 0.11% | 87.5 ± 1.7 |
| 72 | 2025-05-28 | 05:38 | 160 | 15.9 | *H* | −1.66% ± 0.12% | 87.4 ± 1.8 |
| 88 | 2023-07-26 | 09:21 | 160 | 22.1 | *J* | +1.00% ± 0.10% | 0.1 ± 3.0 |
| 88 | 2023-07-26 | 09:30 | 160 | 22.1 | *H* | +0.85% ± 0.10% | 170.1 ± 3.6 |
| 88 | 2023-08-26 | 06:52 | 160 | 12.6 | *J* | −1.02% ± 0.10% | 92.4 ± 2.9 |
| 88 | 2023-08-26 | 07:01 | 160 | 12.6 | *H* | −0.85% ± 0.10% | 87.4 ± 3.4 |
| 88 | 2024-01-29 | 03:03 | 160 | 19.7 | *H* | +0.45% ± 0.12% | 10.6 ± 8.0 |
| 88 | 2024-01-29 | 03:12 | 160 | 19.7 | *J* | +0.33% ± 0.11% | 169.9 ± 12.0 |
| 97 | 2025-03-02 | 09:44 | 160 | 6.1 | *H* | −1.67% ± 0.11% | 89.6 ± 1.7 |
| 97 | 2025-03-02 | 09:52 | 160 | 6.1 | *J* | −1.60% ± 0.11% | 83.3 ± 1.9 |
| 140 | 2023-07-26 | 10:53 | 960 | 25.7 | *J* | −0.14% ± 0.11% | 116.5 ± 20.8 |
| 140 | 2023-07-26 | 11:16 | 960 | 25.7 | *H* | +0.35% ± 0.10% | 0.8 ± 8.7 |
| 140 | 2023-08-26 | 08:30 | 320 | 20.6 | *J* | −0.76% ± 0.11% | 93.7 ± 4.2 |
| 140 | 2023-08-26 | 08:39 | 320 | 20.6 | *H* | −0.72% ± 0.11% | 85.9 ± 4.5 |
| 145 | 2021-11-08 | 07:02 | 1920 | 6.7 | *J* | −1.60% ± 0.10% | 90.2 ± 1.8 |
| 145 | 2021-11-08 | 07:13 | 1920 | 6.7 | *H* | −1.78% ± 0.10% | 92.6 ± 1.6 |

**Table A1**
(Continued)

| Asteroid | Observation Date | UT | Total $t_{\rm exp}$ (s) | Phase (deg) | Filter | $P_r$ | $\theta_r$ |
|---|---|---|---|---|---|---|---|
| 145 | 2023-01-07 | 12:29 | 960 | 23.9 | *J* | +1.25% ± 0.11% | 175.2 ± 2.4 |
| 145 | 2023-01-07 | 12:53 | 960 | 23.9 | *H* | +1.24% ± 0.12% | 178.2 ± 2.4 |
| 145 | 2023-05-16 | 06:43 | 120 | 14.1 | *J* | −1.23% ± 0.14% | 84.1 ± 3.5 |
| 172 | 2024-01-29 | 11:17 | 960 | 15.7 | *J* | −0.88% ± 0.12% | 93.2 ± 3.7 |
| 172 | 2024-01-29 | 11:40 | 960 | 15.7 | *H* | −1.25% ± 0.12% | 83.8 ± 2.4 |
| 173 | 2023-08-26 | 10:48 | 160 | 26.9 | *J* | +2.76% ± 0.11% | 177.2 ± 1.2 |
| 173 | 2023-08-26 | 10:56 | 160 | 26.9 | *H* | +2.16% ± 0.12% | 2.4 ± 1.5 |
| 173 | 2023-11-08 | 12:44 | 160 | 17.0 | *J* | −0.68% ± 0.11% | 87.1 ± 4.4 |
| 173 | 2023-11-08 | 12:52 | 160 | 17.0 | *H* | −0.49% ± 0.12% | 77.1 ± 6.0 |
| 173 | 2024-01-29 | 06:07 | 160 | 19.9 | *J* | +0.22% ± 0.11% | 176.7 ± 15.1 |
| 173 | 2024-01-29 | 06:15 | 160 | 19.9 | *H* | +0.15% ± 0.12% | 6.6 ± 21.8 |
| 173 | 2025-03-02 | 10:01 | 160 | 3.3 | *J* | −1.03% ± 0.13% | 92.3 ± 3.6 |
| 173 | 2025-03-02 | 10:10 | 160 | 3.3 | *H* | −0.99% ± 0.11% | 75.1 ± 4.2 |
| 234 | 2023-07-26 | 06:51 | 160 | 6.7 | *J* | −1.49% ± 0.10% | 89.3 ± 2.0 |
| 234 | 2023-07-26 | 07:00 | 160 | 6.7 | *H* | −1.48% ± 0.10% | 93.2 ± 2.0 |
| 234 | 2023-08-26 | 04:08 | 160 | 18.3 | *J* | −1.46% ± 0.10% | 90.6 ± 2.0 |
| 234 | 2023-08-26 | 04:17 | 160 | 18.3 | *H* | −0.94% ± 0.10% | 91.2 ± 3.1 |
| 269 | 2022-05-31 | 10:52 | 160 | 17.7 | *H* | −0.40% ± 0.10% | 74.4 ± 7.4 |
| 269 | 2022-05-31 | 10:57 | 160 | 17.7 | *J* | −0.35% ± 0.11% | 100.3 ± 8.5 |
| 269 | 2022-07-11 | 08:24 | 160 | 5.7 | *H* | −0.98% ± 0.10% | 89.1 ± 3.1 |
| 269 | 2022-07-11 | 08:29 | 160 | 5.7 | *J* | −1.09% ± 0.10% | 93.7 ± 2.8 |
| 349 | 2019-03-17 | 08:05 | 1500 | 7.2 | *H* | −0.36% ± 0.10% | 89.4 ± 8.0 |
| 349 | 2019-03-17 | 08:51 | 1500 | 7.2 | *J* | −0.45% ± 0.10% | 93.7 ± 6.6 |
| 349 | 2021-06-26 | 11:03 | 160 | 16.6 | *H* | −0.23% ± 0.10% | 94.5 ± 12.7 |
| 349 | 2021-06-26 | 11:08 | 160 | 16.6 | *J* | −0.26% ± 0.10% | 93.9 ± 11.4 |
| 349 | 2021-09-04 | 06:57 | 165 | 10.2 | *H* | −0.39% ± 0.10% | 84.4 ± 7.5 |
| 349 | 2021-09-04 | 07:01 | 160 | 10.2 | *J* | −0.44% ± 0.10% | 91.8 ± 6.7 |
| 349 | 2021-11-08 | 02:24 | 160 | 21.4 | *H* | −0.06% ± 0.10% | 109.4 ± 46.3 |
| 349 | 2021-11-08 | 02:29 | 160 | 21.4 | *J* | +0.19% ± 0.11% | 26.8 ± 15.6 |
| 349 | 2022-10-15 | 08:42 | 160 | 17.4 | *H* | −0.10% ± 0.10% | 108.6 ± 30.4 |
| 349 | 2023-01-07 | 06:46 | 160 | 14.2 | *H* | −0.22% ± 0.10% | 73.5 ± 13.0 |
| 349 | 2023-01-07 | 06:55 | 160 | 14.2 | *J* | −0.24% ± 0.10% | 80.0 ± 12.1 |
| 349 | 2023-01-14 | 05:09 | 160 | 15.9 | *J* | −0.36% ± 0.10% | 87.1 ± 8.2 |
| 349 | 2023-01-14 | 05:18 | 160 | 15.9 | *H* | −0.28% ± 0.10% | 101.6 ± 10.4 |
| 349 | 2024-01-29 | 10:28 | 160 | 10.8 | *J* | −0.40% ± 0.11% | 83.8 ± 7.4 |
| 349 | 2024-01-29 | 10:38 | 160 | 10.8 | *H* | −0.35% ± 0.11% | 93.3 ± 8.4 |
| 387 | 2024-01-29 | 04:26 | 960 | 18.0 | *J* | −1.11% ± 0.11% | 87.5 ± 3.0 |
| 387 | 2024-01-29 | 04:49 | 840 | 18.0 | *H* | −0.71% ± 0.12% | 86.7 ± 5.6 |
| 393 | 2023-05-16 | 10:08 | 140 | 24.9 | *J* | +1.72% ± 0.12% | 9.6 ± 2.0 |
| 393 | 2023-05-16 | 10:16 | 120 | 24.9 | *H* | +1.24% ± 0.12% | 1.6 ± 3.0 |
| 393 | 2023-07-26 | 06:31 | 160 | 18.3 | *J* | −0.56% ± 0.10% | 87.6 ± 5.5 |
| 393 | 2023-07-26 | 06:40 | 160 | 18.3 | *H* | −0.25% ± 0.10% | 83.3 ± 12.0 |
| 393 | 2023-08-26 | 03:48 | 160 | 26.0 | *J* | +2.19% ± 0.10% | 0.4 ± 1.3 |
| 393 | 2023-08-26 | 03:57 | 160 | 26.0 | *H* | +2.20% ± 0.11% | 1.1 ± 1.3 |
| 402 | 2023-07-26 | 07:30 | 160 | 3.4 | *J* | −1.11% ± 0.12% | 89.8 ± 3.1 |
| 402 | 2023-07-26 | 07:39 | 160 | 3.4 | *H* | −0.93% ± 0.12% | 94.9 ± 3.6 |
| 402 | 2023-08-26 | 04:43 | 960 | 9.3 | *J* | −1.91% ± 0.11% | 88.8 ± 1.6 |
| 402 | 2023-08-26 | 05:06 | 960 | 9.3 | *H* | −1.49% ± 0.11% | 90.2 ± 2.2 |

**Note.** The degree of polarization $P_r$ has been rotated so that positive values represent polarization perpendicular to the Sun-asteroid-telescope scattering plane at the time of the observations, and negative values represent polarization in this plane. $\theta_r$ is the measured angle of polarization after correcting for the observed $7\overset{\circ}{.}8$ systematic offset and rotated so that 0° is aligned with the vector perpendicular to the scattering plane.

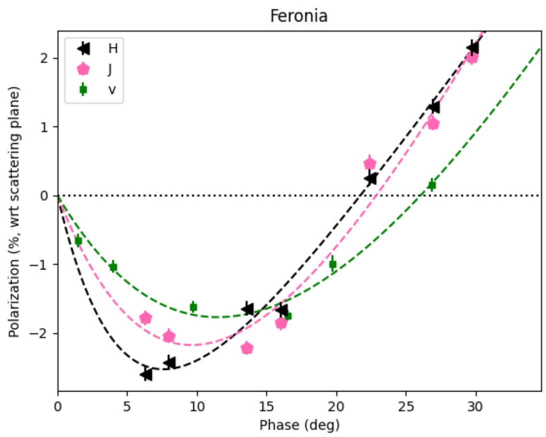


**Figure A1.** The same as Figure 1, showing polarimetric phase curves for T-type asteroid (72) Feronia.

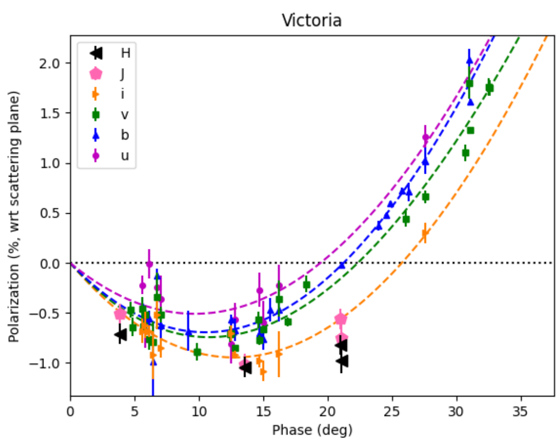


**Figure A2.** The same as Figure 1, showing polarimetric phase curves for S/L-type asteroid (12) Victoria.

## ORCID iDs

Joseph R. Masiero https://orcid.org/0000-0003-2638-720X
Elena Selmi https://orcid.org/0000-0001-7055-4779

## References


Astropy Collaboration, Price-Whelan, A. M., Lim, P. L., et al. 2022, ApJ, 935, 167
Astropy Collaboration, Price-Whelan, A. M., Sipőcz, B. M., et al. 2018, AJ, 156, 123
Astropy Collaboration, Robitaille, T. P., Tollerud, E. J., et al. 2013, A&A, 558, A33
Bach, Y. P., Ishiguro, M., Takahashi, J., et al. 2024, A&A, 684, A80
Bagnulo, S., Belskaya, I., Cellino, A., et al. 2024, A&ARv, 32, 7
Bell, J. F., Davis, D. R., Hartmann, W. K., & Gaffey, M. J. 1989, in Asteroids II, ed. R. P. Binzel, T. Gehrels, & M. S. Matthews (Tucson, AZ: Univ. Arizona Press), 921
Belskaya, I., Cellino, A., Gil-Hutton, R., et al. 2015, in Asteroids IV, ed. P. Michel, F. E. DeMeo, & W. F. Bottke (Tucson, AZ: Univ. Arizona Press), 151
Belskaya, I. N., Fornasier, S., Tozzi, G. P., et al. 2017, Icar, 284, 30
Belskaya, I. N., Levasseur-Regourd, A. C., Cellino, A., et al. 2009, Icar, 199, 97
Bottke, W. F., Nesvorný, D., Grimm, R. E., Morbidelli, A., & O'Brien, D. 2006, Natur, 439, 821
Bradley, L., Sipőcz, B., Robitaille, T., et al. 2019, Astropy/Photutils: v0.7.2, Zenodo, doi:10.5281/zenodo.3568287
Britt, D., Bell, J., Haack, H., & Scott, E. 1992a, LPSC, 23, 167
Britt, D., Bell, J., Haack, H., & Scott, E. 1992b, Metic, 27, 207
Burbine, T. H., McCoy, T. J., Meibom, A., Gladman, B., & Keil, K. 2002, in Asteroids III, ed. W. F. Bottke, Jr. et al. (Tucson, AZ: Univ. Arizona Press), 653
Bus, S. J., & Binzel, R. 2002, Icar, 158, 146
Bus, S. J., Vilas, F., & Barucci, M. A. 2002, in Asteroids III, ed. W. F. Bottke, Jr. et al. (Tucson, AZ: Univ. Arizona Press), 169
Cantillo, D., Reddy, V., Sharkey, B., et al. 2021, PSJ, 2, 95
Carry, B. 2012, P&SS, 73, 98
Clark, B. E., Ockert-Bell, M. E., Cloutis, E. A., et al. 2009, Icar, 202, 119
Coradini, A., Capaccioni, F., Erard, S., et al. 2011, Sci, 344, 492
de Kleer, K., Cambioni, S., Butler, B., et al. 2024, PSJ, 5, 230
de Kleer, K., Cambioni, S., & Shepard, M. 2021, PSJ, 2, 149
DeMeo, F. E., Binzel, R. P., Slivan, S. M., & Bus, S. J. 2009, Icar, 202, 160
Dibb, S. D., Asphaug, E., Bell, J. F., et al. 2024, AGUA, 5, e2023AV001077
Kohout, T., Petrova, E., Yakovlev, G., et al. 2020, A&A, 639A, 146
Lazzaro, D., Angeli, C. A., Carvano, J. M., et al. 2004, Icar, 172, 179
Lupishko, D. 2022, Asteroid Polarimetric Database v2.0, NASA Planetary Data System, doi:10.26033/hyf9-4762
Mahlke, M., Carry, B., & Mattei, P.-A. 2022, A&A, 665, A26
Mainzer, A. K., Bauer, J. M., Cutri, R. M., et al. 2019, NEOWISE Diameters and Albedos v2.0, NASA Planetary Data System, doi:10.26033/18S3-2Z54
Mainzer, A. K., Grav, T., Masiero, J., et al. 2011, ApJ, 741, 90
Masiero, J., DeMeo, F., Kasuga, T., & Parker, A. 2015, in Asteroids IV, ed. P. Michel, F. E. DeMeo, & W. F. Bottke (Tucson, AZ: Univ. Arizona Press), 323
Masiero, J., Devogéle, M., Mascias, I., Castaneda Jaimes, J., & Cellino, A. 2023, PSJ, 4, 93
Masiero, J., Grav, T., Mainzer, A., et al. 2014, ApJ, 791, 121
Masiero, J., Hartzell, C., & Scheeres, D. 2009, AJ, 138, 1557
Masiero, J., Mainzer, A., Bauer, J., et al. 2013, ApJ, 770, 7
Masiero, J., Tinyanont, S., & Millar-Blanchaer, M. A. 2022, PSJ, 3, 90
McFadden, K., Mainzer, A. K., Masiero, J. R., et al. 2025, PSJ, submitted
Mothé-Diniz, T., & Carvano, J. M. 2005, A&A, 442, 727
Mothé-Diniz, T., Carvano, J. M., Bus, S. J., et al. 2008, Icar, 195, 277
Muinonen, K., Penttilä, A., Cellino, A., et al. 2009, M&PS, 44, 1937
Muinonen, K., Piironen, J., Shkuratov, Y. G., Ovcharenko, A., & Clark, B. 2002, in Asteroids III, ed. W. F. Bottke, Jr. et al. (Tucson, AZ: Univ. Arizona Press), 123
Neese, C., Benner, L. A. M., & Ostro, S. J. 2020, Asteroid Radar v1.0, NASA Planetary Data System, doi:10.26033/cqz1-et40
Ostro, S., Hudson, R. S., Nolan, M. C., et al. 2000, Sci, 288, 836
Reddy, V., Sanchez, J., Bottke, W., et al. 2014, Icar, 237, 116
Sanchez, J., Reddy, V., LeCorre, L., Pearson, N., & Battle, A. 2025, PSJ, 6, 69
Sanchez, J., Reddy, V., Shepard, M., et al. 2017, AJ, 153, 29
Sierks, H., Lamy, P., Barbieri, C., et al. 2011, Sci, 334, 487
Sultana, R., Poch, O., Beck, P., et al. 2023a, Icar, 395, 115492
Sultana, R., Poch, O., Beck, P., et al. 2023b, "Polarization Dataset—Reflection, Emission, and Polarization Properties of Surfaces Made of Hyperfine Grains, and Implications for the Nature of Primitive Small Bodies", v1, Zenodo, doi:10.5281/zenodo.7649167
Tinyanont, S., Millar-Blanchaer, M. A., Jovanovic, N., et al. 2019a, Proc. SPIE, 11132, 1113209
Tinyanont, S., Millar-Blanchaer, M. A., Nilsson, R., et al. 2019b, PASP, 131, 25001
Vernazza, P., Lamy, P., Groussin, O., et al. 2011, Icar, 216, 650
Zhang, B., Chabot, N. L., & Rubin, A. E. 2024, PNAS, 121, e2306995121